New Finite-Volume Scheme for Anisotropic Diffusion

Bram van Es [*†], Barry Koren [‡] and Hugo J. de Blank [†]

September 29, 2014

Abstract

In this paper, we propose a special finite-volume scheme to test the importance of connectivity of the finite volumes. We apply the scheme to the anisotropic heat-conduction equation, and compare its results with those of existing finite-volume schemes for anisotropic diffusion. Also, we introduce a model adaptation of the steady diffusion equation for extremely anisotropic diffusion problems with closed field lines.

1 Introduction

Most of the techniques to handle diffusion in anisotropic media are based on finite-volume or finite-element methods and revolve around handling the interpolation of the flux over the cell faces. A lot of work has been done on finite-volume schemes for the solution of diffusion problems on unstructured grids with discontinuous and anisotropic diffusion tensors. Here an important assumption in constructing the formulation of the cell-face fluxes is the continuity of the heat flux over the cell-faces, see for instance Edwards and Rogers [7], Maire et al. [16] and Jacq et al. [12]. Vertex values are used in several cell-centered schemes to approximate the flux over the cell face, see e.g. Le Potier [13], Lipnikov et al. [15], Coudière et al. [5]. The vertex values are approximated with for instance continuity and monotonicity in mind. The vertex values may be defined explicitly but this requires some sort of dual grid, see e.g. Hermeline [10], Le Potier [14], Morel et al. [17]. Shashkov and Steinberg [19] put the flux values in the vertices and then average to the centers of the cell-faces. For a more detailed overview of finite-volume methods the reader is referred to the review paper by Droniou [6]. What motivated Morel et al. [17], Breil and Maire [3], Hyman et al. [11] and others in developing flux(-normal) continuous schemes was grid robustness of finite-volume methods and finite-element methods in case of diffusion-tensor discontinuities. Van Es et al. [22] looked at the importance of alignment for a finite-difference method. In that paper several schemes are compared. The importance of internodal/volume continuity was expected because the formal accuracy for all schemes using series expansions was second order and a decisive effect of lower continuity at the boundaries was not visible in a local error analysis although it clearly mattered in terms of boundary treatment.

In this paper we propose and apply a finite-volume scheme that can change the connectivity between the volumes by changing the length of the cell faces with a free parameter. We apply both cell-face and vertex-centered flux points.

As before we approximate the anisotropic thermal diffusion, described by

$$\mathbf{q} = -\mathbf{D} \cdot \nabla T, \quad \frac{\partial T}{\partial t} = -\nabla \cdot \mathbf{q} + f, \tag{1}$$

[*]Centrum Wiskunde & Informatica, es@cwi.nl, P.O. Box 94079, 1090GB Amsterdam, the Netherlands

[†]FOM Institute DIFFER, Dutch Institute for Fundamental Energy Research, Association EURATOM-FOM, the Netherlands, www.differ.nl

[‡]Eindhoven University of Technology, the Netherlands

where T represents the temperature, $\mathbf{b}$ the unit direction vector of the field line, f some source term and $\mathbf{D}$ the diffusion tensor. The boundary conditions are of Dirichlet type and are discussed per test case.

2 Finite-Volume schemes

All the schemes to be discussed formally have local second-order accuracy, which can be shown by carefully expanding the approximations using Taylor series, see appendix A. However, as can be seen in the results of the test cases discussed in section 4, the accuracy of these methods may drop below their formal accuracy even though the test cases have $\mathcal{C}_\infty$ solutions and source functions. One important aspect that may be overlooked by the local analysis is the continuity between elements, or some equivalent property for finite differences. The symmetric scheme by Günter et al. [9] shows anisotropy independent results in case the diffusion tensor components are captured exactly by the staggered grid points.
The symmetric scheme has $\mathcal{C}_0$ flux values and $\mathcal{C}_1$ temperature values at the flux points, in all directions, i.e. on the dual grid the solution is $\mathcal{C}_1$. Or speaking in finite-volume terms, the values of the solution on the flux points that connect neighbouring control volumes are $\mathcal{C}_1$. The equivalent control volume of the asymmetric scheme, which shows a loss of accuracy and convergence, is only $\mathcal{C}_1$ connected to the control volumes to the left/right and bottom/top, there is no direct connection with the diagonally neighbouring control volumes. To test the hypothesis that continuity between elements is important for the capturing of anisotropic diffusion we adapt the asymmetric finite-volume scheme so that all control volumes are $\mathcal{C}_1$ connected. Both the symmetric and the asymmetric scheme have equivalent finite-volume schemes, the

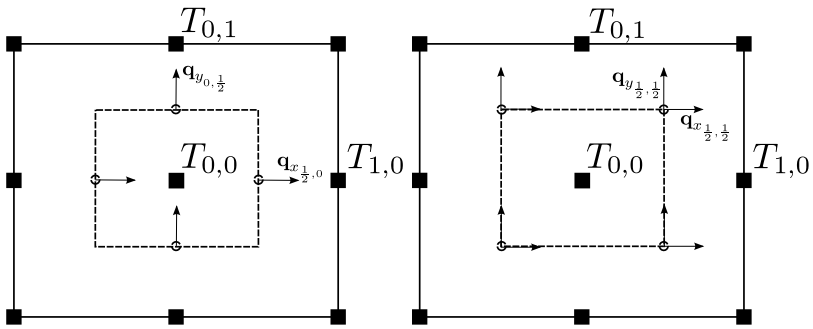

(a) Asymmetric (b) Symmetric

Figure 1: Control volumes, volume contour S indicated by dashed line.

difference now lies in the position of the fluxes on the surface of the control volume, see figure 1. A basic assumption of the finite-volume method is that the solution is spatially constant inside the control volumes. For the diffusion equation

$$T_t = -\frac{1}{V}\oint_S \mathbf{q}\cdot\mathbf{n}dS + \frac{1}{V}\int_V f dV, \quad \mathbf{q} \quad = -\mathbf{D}\cdot\nabla T,$$

we get the same discrete formulation when using finite differences or finite volumes in case of equidistant grids, to be considered here. The mesh sizes are given by $\Delta x = \Delta y = h$. First we discuss the reference methods, namely the asymmetric finite-volume scheme and the symmetric finite-volume scheme.

2.1 Asymmetric finite volume

The first scheme we describe has the flux points defined on the cell-face centers, see figure 1a. We have the following approximations for the gradients on the axes

$$\begin{aligned}
\left.\frac{\partial T}{\partial x}\right|_{i+\frac{1}{2},j} &= \frac{T_{i+1,j} - T_{i,j}}{h}, \\
\left.\frac{\partial T}{\partial y}\right|_{i+\frac{1}{2},j} &= \frac{T_{i+1,j+1} + T_{i,j+1} - T_{i,j-1} - T_{i+1,j-1}}{4h}, \\
\left.\frac{\partial T}{\partial x}\right|_{i,j+\frac{1}{2}} &= \frac{T_{i+1,j+1} + T_{i+1,j} - T_{i-1,j+1} - T_{i-1,j}}{4h}, \\
\left.\frac{\partial T}{\partial y}\right|_{i,j+\frac{1}{2}} &= \frac{T_{i,j+1} - T_{i,j}}{h}.
\end{aligned}$$

For the heat-conduction term we have

$$\begin{aligned}
\mathbf{q}_{i\pm\frac{1}{2},j} &= -\mathbf{D}_{i\pm\frac{1}{2},j} \cdot \left(\left.\frac{\partial T}{\partial x}\right|_{i\pm\frac{1}{2},j}, \left.\frac{\partial T}{\partial y}\right|_{i\pm\frac{1}{2},j} \right)^T, \\
\mathbf{q}_{i,j\pm\frac{1}{2}} &= -\mathbf{D}_{i,j\pm\frac{1}{2}} \cdot \left(\left.\frac{\partial T}{\partial x}\right|_{i,j\pm\frac{1}{2}}, \left.\frac{\partial T}{\partial y}\right|_{i,j\pm\frac{1}{2}} \right)^T.
\end{aligned}$$

Finally, the contour integral of the fluxes is approximated by

$$\oint_S \mathbf{q} \cdot \mathbf{n} dS = \left[\left(\mathbf{q}_{i,j+\frac{1}{2}} - \mathbf{q}_{i,j-\frac{1}{2}} \right) \cdot (0,1) + \left(\mathbf{q}_{i+\frac{1}{2},j} - \mathbf{q}_{i-\frac{1}{2},j} \right) \cdot (1,0) \right] h.$$

2.2 Symmetric finite volume

Another approach is taken by Günter et al. [9], they use a symmetric scheme (with a symmetric linear operator) that is mimetic by maintaining the self-adjointness of the differential operator. The flux points are placed at the vertices of the control volumes. The control volume with the location of the fluxes is given in figure 1b. The divergence terms are determined at the center points in the following manner

$$\begin{aligned}
\left.\frac{\partial T}{\partial x}\right|_{i+\frac{1}{2},j+\frac{1}{2}} &= \frac{T_{i+1,j+1} + T_{i+1,j} - T_{i,j+1} - T_{i,j}}{2h}, \\
\left.\frac{\partial T}{\partial y}\right|_{i+\frac{1}{2},j+\frac{1}{2}} &= \frac{T_{i,j+1} + T_{i+1,j+1} - T_{i+1,j} - T_{i,j}}{2h}.
\end{aligned} \tag{2}$$

Next, the diffusion tensor is applied to obtain the heat flux

$$\begin{aligned}
\mathbf{q}_{i\pm\frac{1}{2},j\pm\frac{1}{2}} &= -\mathbf{D}_{i\pm\frac{1}{2},j\pm\frac{1}{2}} \cdot \left(\left.\frac{\partial T}{\partial x}\right|_{i\pm\frac{1}{2},j\pm\frac{1}{2}}, \left.\frac{\partial T}{\partial y}\right|_{i\pm\frac{1}{2},j\pm\frac{1}{2}} \right)^T, \\
\mathbf{q}_{i\pm\frac{1}{2},j\mp\frac{1}{2}} &= -\mathbf{D}_{i\pm\frac{1}{2},j\mp\frac{1}{2}} \cdot \left(\left.\frac{\partial T}{\partial x}\right|_{i\pm\frac{1}{2},j\mp\frac{1}{2}}, \left.\frac{\partial T}{\partial y}\right|_{i\pm\frac{1}{2},j\mp\frac{1}{2}} \right)^T.
\end{aligned}$$

Finally, the contour integral of the fluxes is approximated by

$$\begin{aligned}
\oint_S \mathbf{q} \cdot \mathbf{n} dS = \frac{1}{2} \Big[&\left(\mathbf{q}_{i+\frac{1}{2},j+\frac{1}{2}} + \mathbf{q}_{i+\frac{1}{2},j-\frac{1}{2}} \right) \cdot (1,0) - \left(\mathbf{q}_{i-\frac{1}{2},j-\frac{1}{2}} + \mathbf{q}_{i+\frac{1}{2},j-\frac{1}{2}} \right) \cdot (0,1) \\
&+ \left(\mathbf{q}_{i+\frac{1}{2},j+\frac{1}{2}} + \mathbf{q}_{i-\frac{1}{2},j+\frac{1}{2}} \right) \cdot (0,1) - \left(\mathbf{q}_{i-\frac{1}{2},j-\frac{1}{2}} + \mathbf{q}_{i-\frac{1}{2},j+\frac{1}{2}} \right) \cdot (1,0) \Big] h.
\end{aligned}$$

2.3 Eight point flux scheme

To investigate the importance of flux continuity and connectivity we apply a cell-face-centered flux (CF) scheme and a vertex-centered flux (VF) scheme on a grid with varying connectivity. The grid is varied

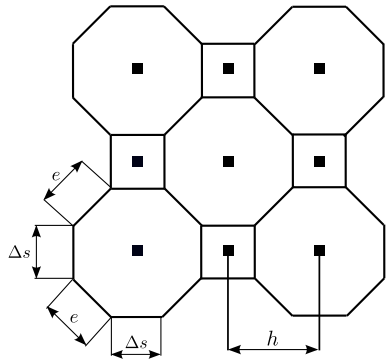

Figure 2: Part of hybrid grid ($0 < e < \sqrt{2}h$).

through a parameter e, $e \in [0, \sqrt{2}h]$, where for $e = 0$ and $e = \sqrt{2}h$ the grid is uniform and rectangular, and for e between 0 and $\sqrt{2}h$ we have a hybrid grid consisting of octogonals with edges of lengths e and Δs and squares with edge length Δs (figure 2).

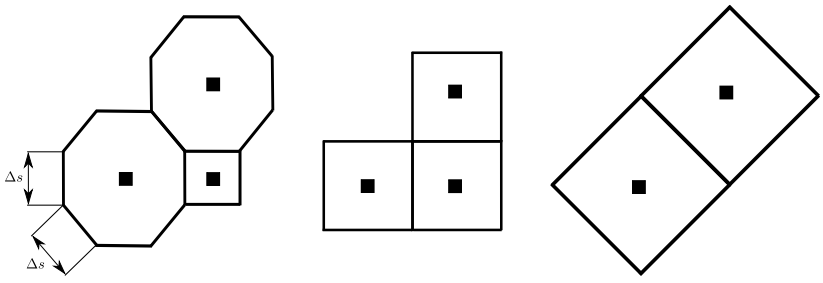

Figure 3: (a) $e = \Delta s$, (b) $e = 0$, (c) $e = \sqrt{2}h$.

Note that it holds $\Delta s = h - e/\sqrt{2}$, and hence, with all edges of the same length, $e = \Delta s$, $\Delta s = (2 - \sqrt{2})h$. The latter situation has been depicted in figure 3a. The two extreme cases $e = 0$ and $e = \sqrt{2}h$ are given in figures 3b and 3c, respectively. Note that in the case of $e = \sqrt{2}h$ the grid may be better aligned to features that are oblique with respect to the coordinate axes, but it will be coarser and have less finite volumes. For each volume we approximate the contour integral of the fluxes as follows

$$\oint_S \mathbf{q} \cdot \mathbf{n} dS \approx \sum_{i=1}^{M} \tilde{\mathbf{q}}_i \cdot \mathbf{n}_i \, l_i,$$

where $\tilde{\mathbf{q}}_i$ is an approximation of the flux across cell face i, and where $M = 4$ and $M = 8$ for the square and octogonal finite volume, respectively. Extending this approach to three dimensions is straightforward for a uniform Cartesian grid.

2.3.1 Vertex-centered fluxes

The VF scheme has the following description of the divergence

$$\begin{aligned}\text{Octogonal volume:}\quad \oint_S \mathbf{q}\cdot\mathbf{n}dS &= \frac{1}{2}\sqrt{2}\left[\left(\overline{\mathbf{q}}_{ur,ru}-\overline{\mathbf{q}}_{ld,dl}\right)\cdot(1,1)+\left(\overline{\mathbf{q}}_{rd,dr}-\overline{\mathbf{q}}_{ul,lu}\right)\cdot(1,-1)\right]e \\ &\quad+\left[\left(\overline{\mathbf{q}}_{ru,rd}-\overline{\mathbf{q}}_{lu,ld}\right)\cdot(1,0)+\left(\overline{\mathbf{q}}_{ul,ur}-\overline{\mathbf{q}}_{dl,dr}\right)\cdot(0,1)\right]\Delta s, \qquad (3)\\ \text{Square volume:}\quad \oint_S \mathbf{q}\cdot\mathbf{n}dS &= \left[\left(\overline{\mathbf{q}}_{ru,rd}-\overline{\mathbf{q}}_{lu,ld}\right)\cdot(1,0)+\left(\overline{\mathbf{q}}_{ru,lu}-\overline{\mathbf{q}}_{rd,ld}\right)\cdot(0,1)\right]\Delta s,\end{aligned}$$

where we have to retain the normality of the resulting unit direction vector for the averaging of the fluxes.

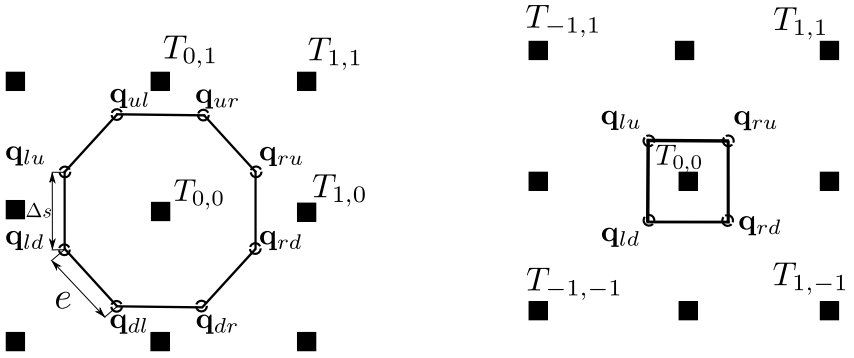

(a) Octogonal volume

(b) Square volume

Figure 4: Control volumes with vertex centered fluxes, contour S indicated by solid line.

The averaged flux vectors $\overline{\mathbf{q}}_{ur,ru}, \overline{\mathbf{q}}_{ul,lu}, \cdots$ generally denoted as $\overline{\mathbf{q}}_{A,B}$, are computed as

$$\overline{\mathbf{q}}_{A,B} = \frac{1}{4}\left[\left((D_{\parallel})_A+(D_{\parallel})_B-(D_{\perp})_A-(D_{\perp})_B\right)\left(\mathbf{b}\mathbf{b}^T\right)_{A,B}+\left((D_{\perp})_A+(D_{\perp})_B\right)\mathcal{I}\right]\left(\nabla T_A+\nabla T_B\right),$$

with $\mathbf{b}_{A,B} = (\mathbf{b}_A+\mathbf{b}_B)/|\mathbf{b}_A+\mathbf{b_B}|$. Here the gradient approximations follow from the interpolation, see figure 4 for the nomenclature. Note that applying a separate normalized averaging of the unit direction vectors gives a division by zero if the unit direction vectors are opposed. In this case we simply have to pick one of the directions, or, if we know that an opposed direction means there is an O-point, we can set the respective parallel flux to zero. Almost directly opposed field lines are numerically not an issue for the normalisation. With O-point we refer to the center of rotation of closed field lines, exactly at the O-point the direction is not defined.

In case of diffusion tensor values not defined exactly in the flux points but rather in the cells, or in case of sharply varying densities, harmonic averaging is preferred for the tensor values on the cell faces (see Edwards and Rogers [7] and Sharma and Hammett [18]). This is generally not the case, e.g. for MHD simulations of fusion plasmas where the density and the diffusion tensor vary smoothly. For this reason we do not consider piecewise constant diffusion tensors, rather we apply a continuous nine-point interpolation. We define the diffusion tensor values exactly in the flux evaluation points.

2.3.2 Cell-face centered fluxes

With the flux vectors in the corner points of the control volume pointing in a direction of 45° with respect to the coordinate axes, the scheme is written as

$$\text{Octogonal volume:} \quad \oint_S \mathbf{q}\cdot\mathbf{n}dS = \left[\frac{1}{2}\sqrt{2}\left((\mathbf{q}_{c_1}-\mathbf{q}_{c_3})\cdot(1,1)+(\mathbf{q}_{c_2}-\mathbf{q}_{c_4})\cdot(1,-1)\right)e \right.$$
$$\left. +\left((\mathbf{q}_r-\mathbf{q}_l)\cdot(1,0)+(\mathbf{q}_u-\mathbf{q}_d)\cdot(0,1)\right)\Delta s\right], \tag{4}$$
$$\text{Square volume:} \quad \oint_S \mathbf{q}\cdot\mathbf{n}dS = \left[(\mathbf{q}_r-\mathbf{q}_l)\cdot(1,0)+(\mathbf{q}_u-\mathbf{q}_d)\cdot(0,1)\right]\Delta s,$$

where the cell-face fluxes $\mathbf{q}_{c_1},\mathbf{q}_{c_2},\mathbf{q}_{c_3},\mathbf{q}_{c_4}$ and $\mathbf{q}_r,\mathbf{q}_l,\mathbf{q}_u,\mathbf{q}_d$ are given in figure 5. Using a circle with radius $\frac{1}{2}\sqrt{2}h$ we ensure that the flux points c_1,c_2,c_3,c_4 lie exactly on the average points of the four surrounding nodes (see figure 5). For the x- and y-derivatives in the vertical and horizontal flux points respectively we

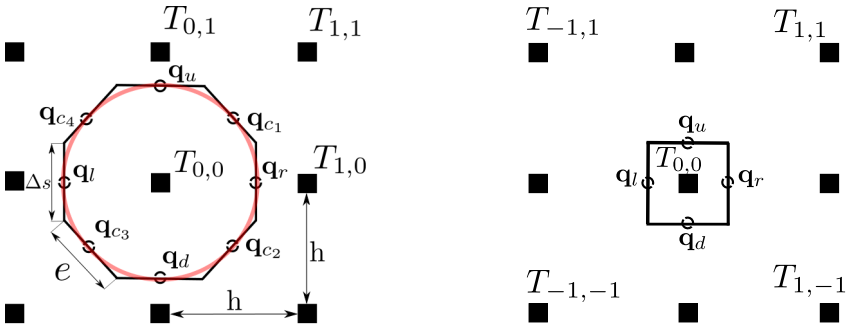

(a) Octogonal volume (b) Square volume

Figure 5: Control volumes with cell-face centered fluxes, contour S indicated by solid line.

use a nine-point interpolation scheme for the temperature, see section 3. For $e = 0$ the scheme reduces to the asymmetric scheme from section 2.1. For $e = \sqrt{2}h$ we end up with a symmetric description for the derivatives. This is equivalent to the symmetric scheme from section 2.2 if we use symmetric approximations for the derivatives. For verification we will also show the results for the asymmetric and symmetric schemes from sections 2.1 and 2.2 respectively.

3 Interpolation for fluxes

Given the formulation of the discrete divergence for the VF and CF scheme we need to find the discrete description of the fluxes. We discuss the use of a local and a non-local flux approximation.

3.1 Multi-point flux approximation for eight point flux scheme

Suppose we apply a local multi-point flux interpolation with the volumes surrounding the flux point, assuming we have cell-centered temperature values. Just like the Multi-Point Flux Approximation (MPFA) method the flux through the interfaces is determined using subcell-descriptions of the temperature. Here triangles may be formed by connecting the center points of three neighbouring volumes, see figure 6. We need two triangles for the determination of one edge flux, as per triangle we determine half of the flux going through the edge (see figure 7). We consider the approach described in e.g. Aavatsmark et al. [1,2] and Edwards and Rogers [7], i.e. we consider subcells with one temperature value per subcell face. Unlike the MPFA-methods, we do not have cellcentered diffusion tensors, but rather edge centered or vertex centered diffusion tensor

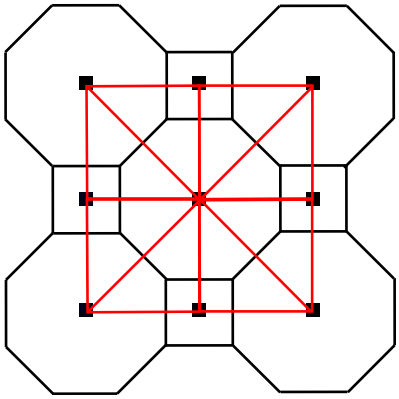

Figure 6: Interaction triangles, indicated by red lines

values. We have already surrounded each vertex with an interaction triangle, which connects the surrounding temperature unknowns. The octogonal volume has eight vertices and thus eight interaction triangles, the square volume has four. It is clear that using a mixture of octogonals and squares for the finite volumes

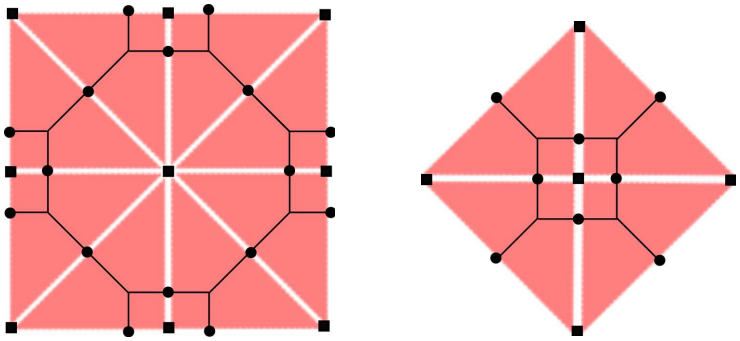

(a) (b)

Figure 7: Interaction triangles for (a) octogonal volume, (b) square volume, solid squares (■) indicate temperature unknowns and solid circles (•) indicate added unknowns to solve for the fluxes.

leads to a mixture of nine-point stencils and five-point stencils when applying a locally conservative method (see figure 7). Only for $e = \sqrt{2}h$ and $e = 0$ a nine-point stencil emerges. It is known from literature that to properly resolve non-grid-aligned anisotropic diffusion with a linear scheme at least a nine-point stencil is required (see e.g. Umansky et al. [21]). The five-point stencil for the square volumes, which is unavoidable when using a combination of octogonal and square volumes, does not satisfy this requirement. Hence we will not further consider this multi-point flux approach.

3.2 Non-local flux approximation

Since the flux points r, l, u, d are off-center with respect to the centered temperature values we are forced to involve more points to obtain second-order accuracy in approximating the derivatives in these flux points. To have second-order accuracy for general values of e we apply biquadratic interpolation of the surrounding temperature values. When applying a nine-point interpolation we are assuming to have a continuous temperature and flux distribution. In case of a smoothly varying diffusion tensor and temperature value this assumption is realistic. Also see the Center Flux Scheme by Ferziger and Peric [8].

We have the following description for the derivatives:

$$\begin{aligned}\left.\frac{\partial T}{\partial x}\right|_{x,y} &\approx F(x,y) = \frac{\partial}{\partial x}\sum_{i=0}^{2}\sum_{j=0}^{2}\gamma_{ij}x^i y^j,\\ \left.\frac{\partial T}{\partial y}\right|_{x,y} &\approx G(x,y) = \frac{\partial}{\partial y}\sum_{i=0}^{2}\sum_{j=0}^{2}\gamma_{ij}x^i y^j,\end{aligned} \tag{5}$$

where the set of coefficients γ_{ij} is found by applying the Vandermonde matrix to the cell-centered temperature unknowns and subsequently differentiating the interpolation function, see appendices B and C. A second option is to weigh the symmetric approximation of the derivatives given e.g. by equation(2) such that the derivatives are given by

$$\begin{aligned}T_x \approx& \alpha_{ru}\frac{T_{i+1,j+1}+T_{i+1,j}-T_{i,j+1}-T_{i,j}}{2h} + \alpha_{lu}\frac{T_{i,j}+T_{i,j+1}-T_{i-1,j+1}-T_{i-1,j}}{2h}\\ &+\alpha_{ld}\frac{T_{i,j}+T_{i,j-1}-T_{i-1,j}-T_{i-1,j-1}}{2h} + \alpha_{rd}\frac{T_{i+1,j}+T_{i+1,j-1}-T_{i,j}-T_{i,j-1}}{2h},\\ T_y \approx& \alpha_{ru}\frac{T_{i+1,j+1}+T_{i,j+1}-T_{i,j}-T_{i+1,j}}{2h} + \alpha_{lu}\frac{T_{i,j+1}+T_{i-1,j+1}-T_{i-1,j}-T_{i,j}}{2h}\\ &+\alpha_{ld}\frac{T_{i,j}+T_{i-1,j}-T_{i-1,j-1}-T_{i,j-1}}{2h} + \alpha_{rd}\frac{T_{i+1,j}+T_{i,j}-T_{i,j-1}-T_{i+1,j-1}}{2h}.\end{aligned} \tag{6}$$

These derivatives are consistently summed in a weighted fashion, where the weights are given by

$$\begin{aligned}\alpha_{ru} &= \left(\frac{1}{2}+\frac{x}{h}\right)\left(\frac{1}{2}+\frac{y}{h}\right),\\ \alpha_{lu} &= \left(\frac{1}{2}-\frac{x}{h}\right)\left(\frac{1}{2}+\frac{y}{h}\right),\\ \alpha_{rd} &= \left(\frac{1}{2}+\frac{x}{h}\right)\left(\frac{1}{2}-\frac{y}{h}\right),\\ \alpha_{ld} &= \left(\frac{1}{2}-\frac{x}{h}\right)\left(\frac{1}{2}-\frac{y}{h}\right).\end{aligned} \tag{7}$$

We call the resulting coefficients *locally symmetric*, see appendix C for the contribution to the linear operator.

4 Numerical results and methodological adaptations

In the following test case we will consider both Vandermonde and locally symmetric coefficients. If results are similar we only show the results for the Vandermonde coefficients.

4.1 Closed field-line test cases

In this section we show the results for closed field-line test cases with extreme levels of anisotropy. In this test case $\mathbf{b}\cdot\nabla T = 0$. We vary the values of the parameters e and ς. The test cases we consider have continuous distributions for the diffusion tensor and the temperature. The error norm is defined by

$$\epsilon_\infty = \frac{|\tilde{T}-T|_{max}}{|T|_{max}},$$

where $\tilde{T}$ is the approximate temperature. The problem is considered on a square domain, described by $-0.5 \leq x, y \leq 0.5$. The following steady-state solution is assumed on the domain:

$$T(x,y) = 1-(x^2+y^2)^{3/2}, \tag{8}$$

with the unit direction vector given by

$$\mathbf{b} = \frac{1}{\sqrt{x^2+y^2}} \begin{pmatrix} -y \\ x \end{pmatrix}.$$

In figure 8, we study the accuracy of the various schemes for two anisotropic cases, one being extremely

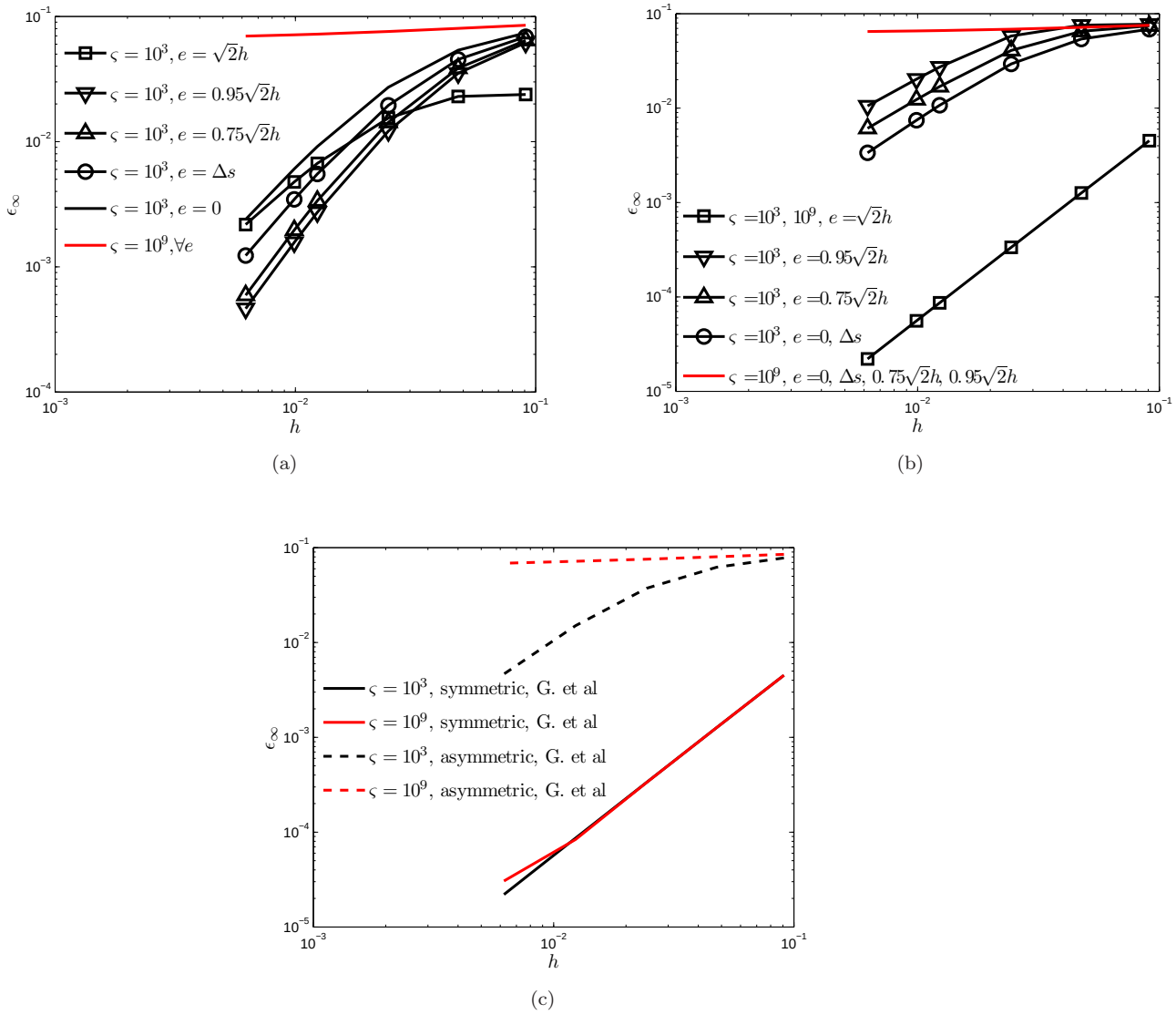

Figure 8: Error ϵ_∞ for anisotropy ratios $\varsigma = 10^3$ and $\varsigma = 10^9$, CF scheme with (a) Vandermonde coefficients, (b) locally symmetric coefficients, and (c) the asymmetric and symmetric scheme of Günter et al.

anisotropic, $\varsigma = 10^9$. The main observation to be made from figure 8 is that for the extremely anisotropic $\varsigma = 10^9$ case only the symmetric scheme by Günter et al. and the CF scheme, with $e = \sqrt{2}h$ and locally symmetric coefficients, are second-order convergent and moreover of low error magnitude. Using the locally symmetric coefficients; for $e \to \sqrt{2}h$ we go from a non-local interpolation involving all the temperature unknowns for each derivative to a local interpolation involving only the volumes surrounding the flux points.

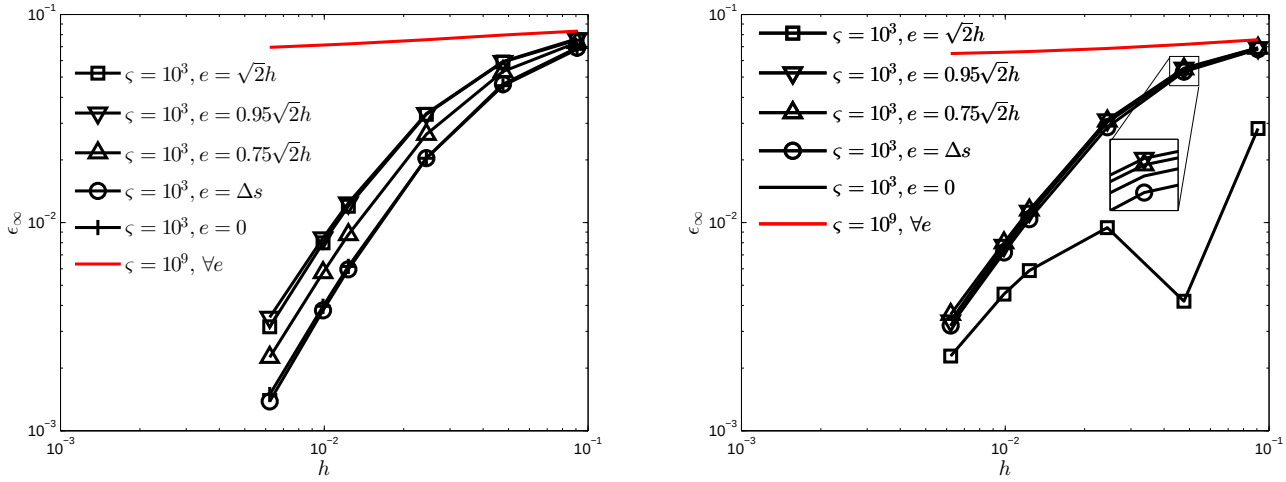

Figure 9: Error ϵ_∞ for anisotropy ratios $\varsigma = 10^3$ and $\varsigma = 10^9$, VF scheme with (a) Vandermonde coefficients, (b) locally symmetric coefficients.

This explains the jump in (order of) accuracy going from $e = 0.95\sqrt{2}h$ to $e = \sqrt{2}h$ in figure 8b. In figure 9 we still present results obtained with the VF scheme for the same test case. Here, as opposed to the CF scheme with locally symmetric coefficients (figure 8), the VF scheme with locally symmetric coefficients does not perform well for $\varsigma = 10^9$.

4.2 e-dependency

We proceed by studying the e-dependency in more detail. We consider a constant angle test case which is described by

$$T(x, y) = xy \left[\sin(\pi x) \sin(\pi y)\right]^{10}, \quad x, y \in [0, 1],$$

where the angle of misalignment α is set to a constant value. The solution simulates a temperature peak. For both the cell face-centered scheme and the vertex-centered scheme we observe a noticeable influence of the dominant angle of anisotropy on the e-dependency of the error, see figure 10. Concerning the effect of e-variation, notice the opposite behavior of the VF scheme and the CF scheme. Also note that for most values of e the error increases as the dominant angle of anisotropy goes to 45°. At and near $e = \sqrt{2}h$, for the CF scheme the behavior is opposite though; CF scheme's best results are obtained for $\alpha = 45°$. For the CF scheme, we also clearly observe the best behavior is at or near $e = \sqrt{2}h$.

4.3 Adaptations for closed field lines

There is a clear distinction between closed and open field-line cases. The closed field-line cases allow for specific adaptations to improve the accuracy. The common point around which the field lines rotate is called the O-point.

4.3.1 Topology mimicking

To incorporate the closed field-line topology in the finite-volume discretisation we enforce that the unit direction vectors are tangential to the edges of the finite volume, see figure 11. Also note that in this

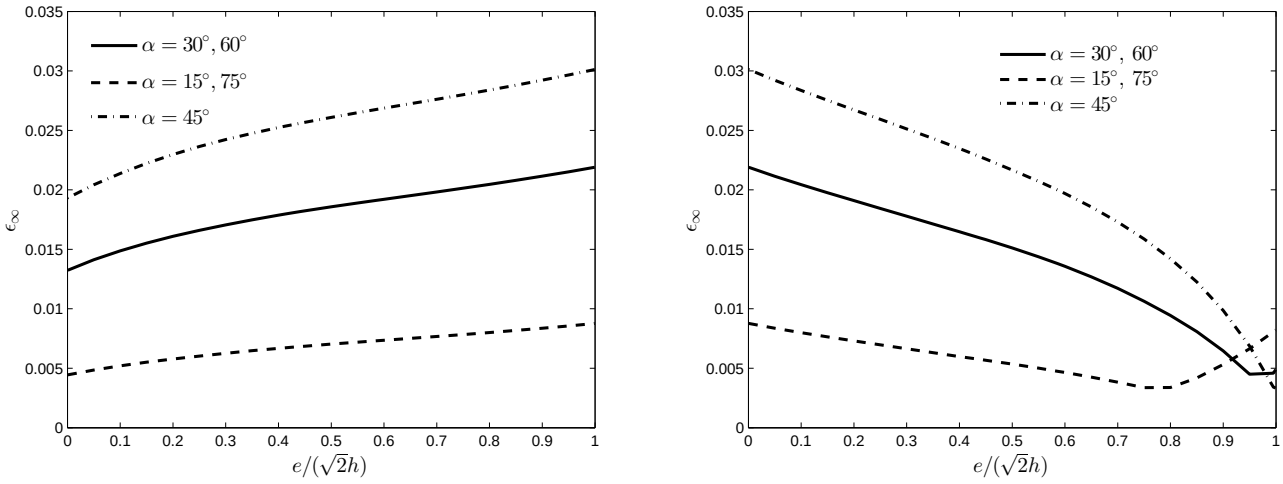

Figure 10: Error ϵ_∞ for constant angle test case, $\varsigma = 10^9$, 50×50 grid and varying values of e, (a) VF scheme, (b) CF scheme.

way we enforce that $\nabla \cdot \mathbf{b} = 0$. In general this is not consistent with the diffusion equation because in general $\nabla \cdot \mathbf{b} \neq 0$. Sovinec et al. [20] devised a test containing only closed field lines to directly compare

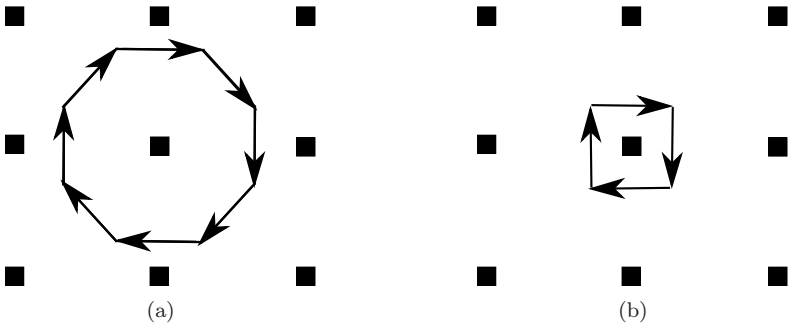

Figure 11: Topology local field lines for (a) octogonal volume, (b) quadrilateral volume.

the perpendicular numerical diffusion to the actual numerical diffusion. The exact solution and the forcing function are given by

$$T = \frac{1}{D_\perp}\psi, \quad f = 2\pi^2\psi, \quad \psi = \cos(\pi x)\cos(\pi y), \quad x, y \in [-0.5, 0.5]. \tag{9}$$

The error in the perpendicular diffusion is given by $|T(0,0)^{-1} - D_\perp|$. We use homogeneous Dirichlet boundary conditions. The field lines are tangential to the contours of constant temperature, i.e.

$$\mathbf{b} = \frac{1}{\sqrt{\psi_x^2 + \psi_y^2}} \begin{pmatrix} -\psi_y \\ \psi_x \end{pmatrix}.$$

We obtain *fourth-order* convergence for the Sovinec test case *independent* of the level of anisotropy, using Vandermonde coefficients, with $e = \sqrt{2}h$, with vertex averaged gradients and with the unit direction vectors enforced to be tangent to the cell faces, see figure 12a. The Sovinec test case has closed field lines, as such

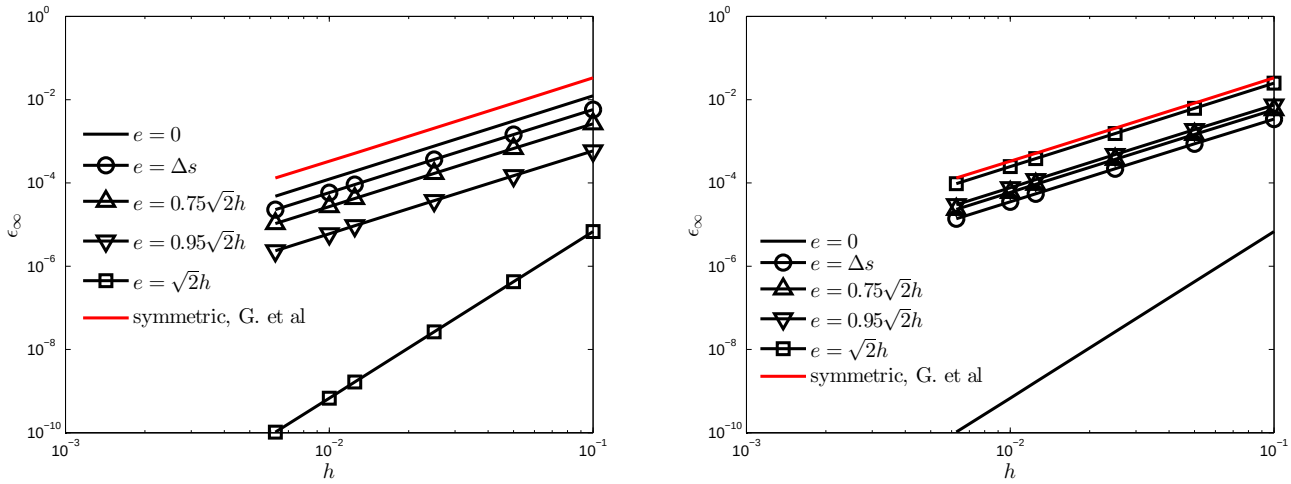

Figure 12: Error ϵ_∞ for Sovinec test case, $\varsigma = 10^9$, with varying values of e, using Vandermonde coefficients. Here the symmetric scheme by Günter et al. is used as a reference. (a) VF scheme, (b) CF scheme.

the topology of the entire domain is mimicked by the individual volumes. We believe this is key to the high-order approximation. We see that the accuracy increases monotonously as e goes to $\sqrt{2}h$, and that it seems to jump to fourth-order for $e = \sqrt{2}h$. Further, we see the inverse for the CF scheme, where we have fourth-order accuracy for $e = 0$ and second order for higher values of e, with a subsequent decrease in accuracy for increasing e, see figure 12b.
The VF scheme with exact unit direction vectors and the VF scheme with averaged unit direction vectors are identical since the local values for the unit direction vector (and thus also its approximation) do not play a role in the accuracy. We note that using the locally symmetric coefficients the results are almost identical, without the fourth-order convergence for $e = \sqrt{2}h$.

If we force the field lines for the parallel diffusion coefficient to be tangential to the cell faces, letting the field lines for the perpendicular diffusion coefficient untouched, we get the same result as setting $D_\parallel$ to zero everywhere in the domain for any level of anisotropy without the fourth-order accuracy for $e = \sqrt{2}h$.

4.3.2 Importance of O-point

We now apply the VF and CF scheme to the Sovinec test case, without the foregoing enforcement of field line topology. We notice a huge difference between odd and even numbered grids; both the VF and the CF scheme perform much better on odd-numbered grids than on even-numbered grids. On the odd-numbered grids, for both schemes, the error of the perpendicular diffusion remains fairly constant with increasing anisotropy, see figure 13.

The gain in accuracy is caused by the fact that the central volume exactly mimicks the topology of the closed field line with $\mathbf{b} \cdot \nabla T = 0$ leading to a zero contribution of $D_\parallel$. To verify this we enforce $D_\parallel = 0$ for the flux points positioned closest to the O-point for the even-numbered grids. The results, given in figure 14, show that enforcing $D_\parallel = 0$ close to the O-point has a similar effect as having a volume exactly on the O-point.

For both the VF scheme and the CF scheme we get $\mathcal{O}(h^4)$ convergence for $e \to \sqrt{2}h$ and $e \to 0$ respectively for the isotropic case if we have a finite volume exactly on the O-point, see figure 15c. The

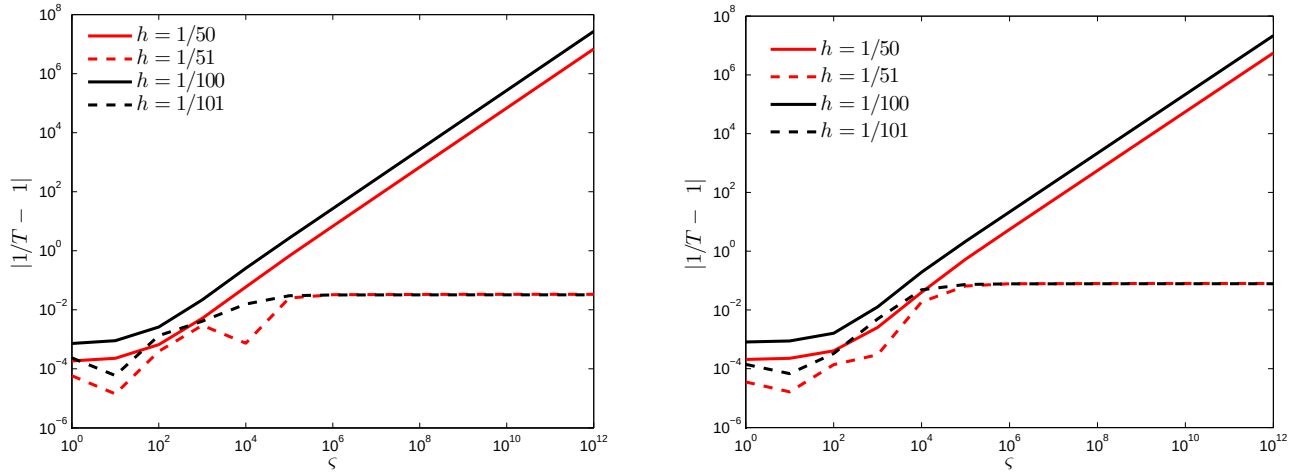

Figure 13: Error $|T^{-1} - 1|$ for Sovinec test case with varying anisotropy, $e = \Delta s$, Vandermonde coefficients, with odd and even number of finite volumes (a) VF scheme, (b) CF scheme.

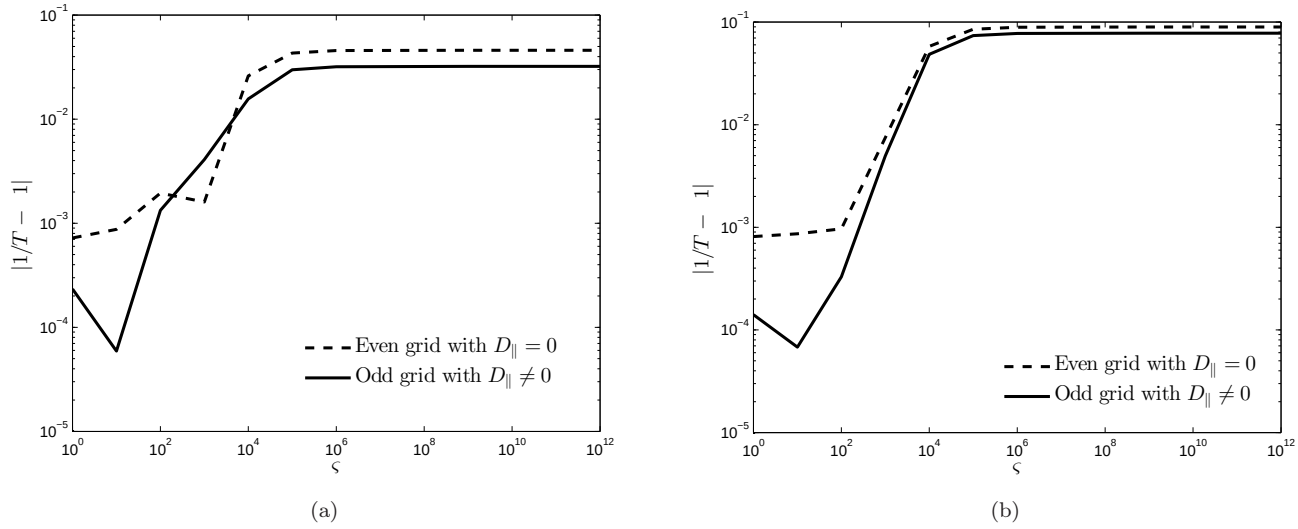

Figure 14: Error $|T^{-1} - 1|$ for Sovinec test case for varying anisotropy for $e = \Delta s$, Vandermonde coefficients, odd and even grid with $D_{\|} \neq 0$ and $D_{\|} = 0$, respectively (a) VF scheme , (b) CF scheme.

4^{th}-order convergence becomes independent of the level of anisotropy if we mimick the topology everywhere in the domain as we saw in section 4.3.

4.3.3 Enforcing $D_{\|} = 0$

We see that enforcing $D_{\|} = 0$ around the O-point, as well as placing a volume exactly on the O-point leads to a considerable gain in accuracy for the Sovinec test case. This approach is interesting as a means to improve existing methods because the location of the O-point can be derived from the magnetic field data. The same

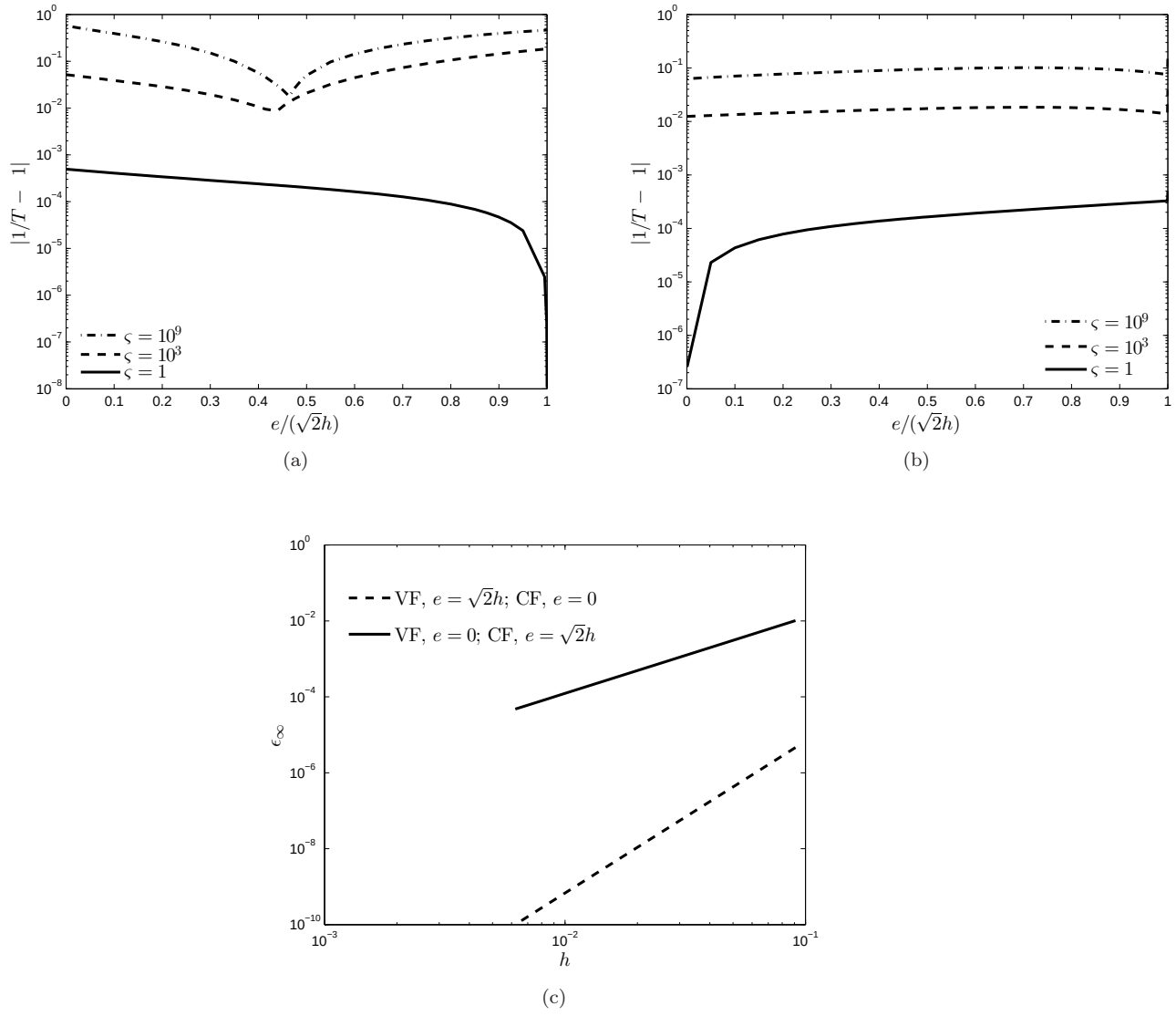

Figure 15: Sovinec test case, Error $|T^{-1} - 1|$ for varying e with anisotropy $\varsigma = 1, 10^3, 10^9$, $N = 51$, Vandermonde coefficients (a) VF scheme, (b) CF scheme, (c) convergence of error ϵ_∞ for $\varsigma = 1$.

caveat as for the topology mimicking holds here; validity is limited to situations where the parallel flux is zero. However, it is not necessarily limited to steady cases. The involvement with the problem parameter $D_\parallel$ might be seen as a form of model reduction. If a point on the last closed field line is found and subsequently $D_\parallel$ is enforced to be zero on the line connecting the outer point and the O-point (see figure 16), we now have full second-order accuracy for $e = 0, e = \Delta s$ and $e = \sqrt{2}h$, see figure 17. We know from Van Es et al. [22] that the symmetric scheme by Günter et al. loses anisotropy independence for tilted elliptic temperature distributions. Note that the symmetric scheme is identical to the symmetric finite volume scheme for a uniform rectangular grid. This tilted elliptic distribution has no symmetry axes aligned with the coordinate axes and as such is more general than the previous test case.

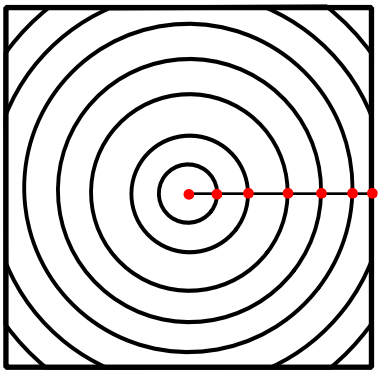

Figure 16: Points where we set $D_{\|}$ to zero.

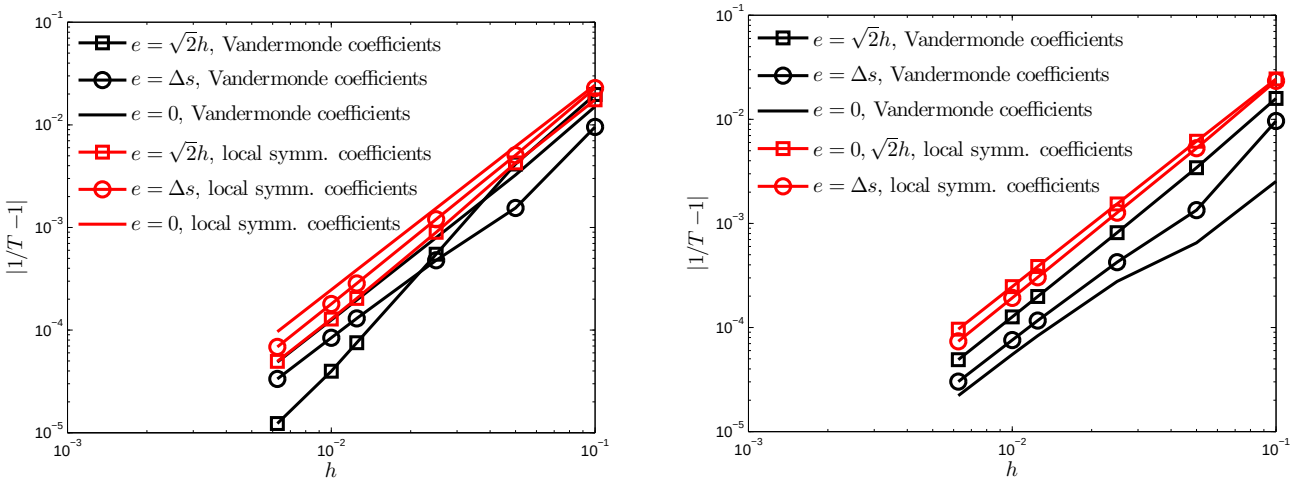

Figure 17: Convergence of $|T^{-1} - 1|$ for Sovinec test case with $\varsigma = 10^9$, (a) VF scheme , (b) CF scheme.

The distribution for the tilted test case is given by

$$T(x, y) = 1 - (a^2(x\cos\theta + y\sin\theta)^2 + b^2(x\sin\theta - y\cos\theta)^2)^{3/2}, \quad x, y \quad \in [-0.5, 0.5], \tag{10}$$

with $\mathbf{b}$ given by

$$\mathbf{b} = \frac{1}{\sqrt{T_x^2 + T_y^2}} \begin{pmatrix} -T_y \\ T_x \end{pmatrix},$$

which ensures that $\mathbf{b} \cdot \nabla T = 0$. First we set $D_{\|} = 0$ on a vertical line through the O-point. Second-order accuracy is obtained for $e = 0$ using the VF scheme, see figure 18. Continuing with $e = 0$ we try different enforcements of $D_{\|} = 0$, from enforcement in the O-point only to enforcement along the full vertical. Second-order accuracy convergence for the VF scheme is obtained completely when we set $D_{\|}$ to zero on the line $x = 0, y > -0.5$ through the origin and likewise for $D_{\|}$ set to zero on the line $x = 0, y > 0$, see figure 19. For an enforcement along the line $x = 0, 0 < y < 0.2$ stagnation of convergence sets in for a moderate resolution. In general the stagnation of convergence is delayed further for a longer line of $D_{\|} = 0$ enforcement. An

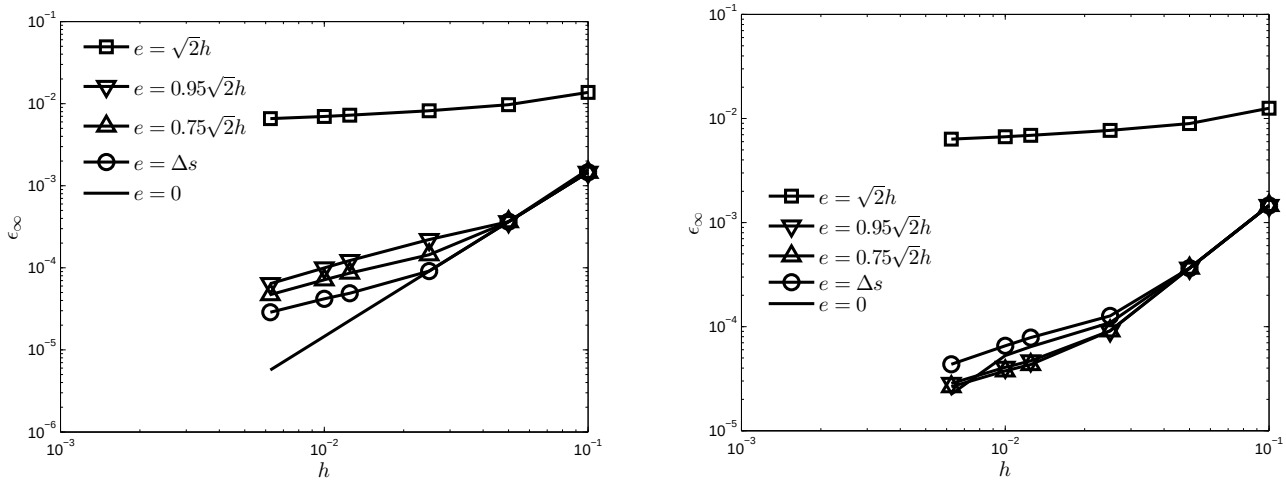

(a) (b)

Figure 18: Convergence of ϵ_∞ for the tilted elliptic test case with $D_\parallel$ set to zero on vertical line through origin, for varying e, $\varsigma = 10^9, \theta = 1/3\pi, a = 0.15, b = 0.85$, Vandermonde coefficients, (a) VF scheme , (b) CF scheme.

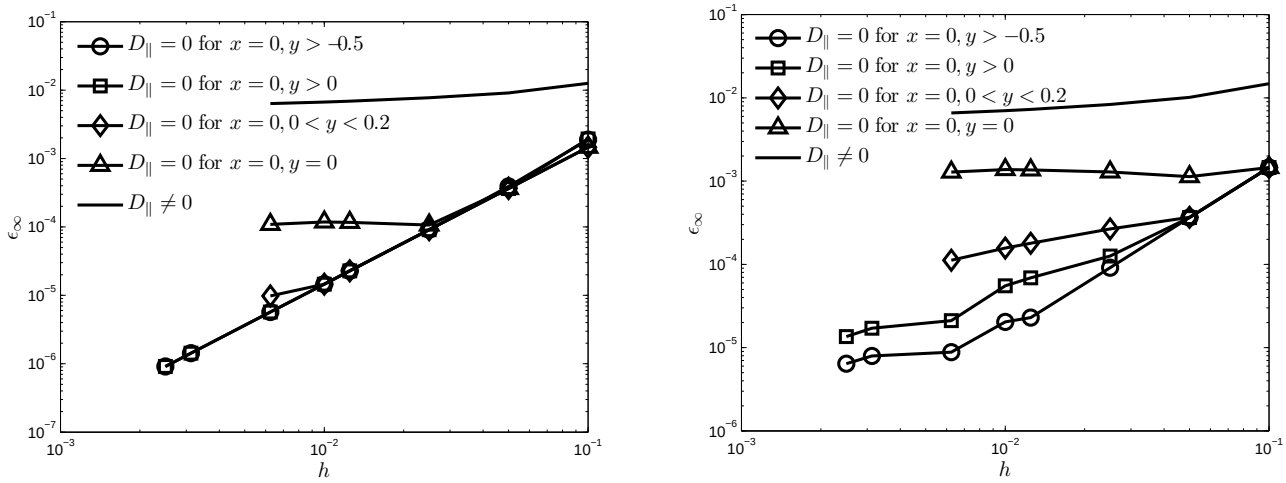

(a) (b)

Figure 19: Convergence of ϵ_∞ for the tilted elliptic test case for $e = 0$, $\varsigma = 10^9, \theta = 1/3\pi, a = 0.15, b = 0.85$, Vandermonde coefficients, (a) VF scheme , (b) CF scheme.

explanation for this is that the longer we make this line of enforcement, the more closed field lines we are able to resolve. This explains the fact that we do not see an improvement for $D_\parallel = 0$ on the full vertical line compared to the half vertical line for the VF scheme since for both $x = 0, y > -0.5$ and $x = 0, y > 0$ we treat all the closed field lines. The results for the CF scheme also improve, but there is no full recovery of the second-order accuracy. Here we should note that for $e = 0$ the only difference between the CF scheme and the VF scheme is the treatment of the temperature gradients. Finally we apply the $D_\parallel = 0$ enforcement on the line $x = 0, y > 0$ to the test case given by equation(8). Comparing the convergence results shown in figure 20 to those in figures 8, 9 we see a full anisotropy independent recovery of the convergence for

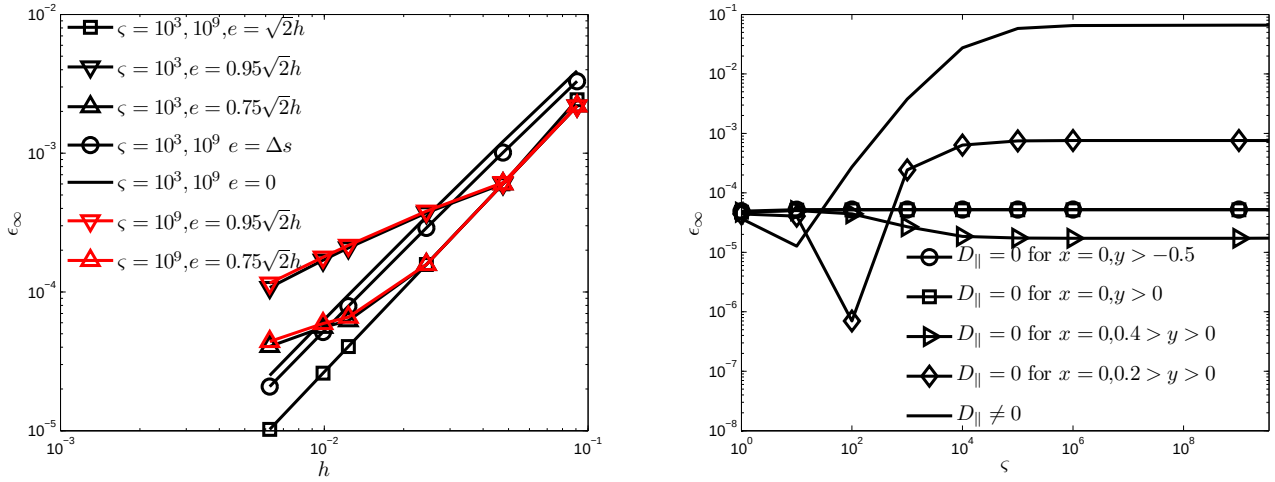

(a) (b)

Figure 20: Error ϵ_∞ for test case with solution(8) using the VF scheme with Vandermonde coefficients, (a) convergence with $\varsigma = 10^9$ and $D_\parallel = 0$ on $x = 0, y > 0$, (b) anisotropy dependency on 100×100 grid with $e = \Delta s$.

$e = 0, \Delta s, \sqrt{2}h$.

4.3.4 Enforcing $D_\parallel = 0$ unsteady

To further test the influence of the closed field line adaptations discussed in section 4.3 we approximate the unsteady diffusion equation with a zero initial condition and a source function that produces the Sovinec distribution, i.e. the exact final temperature distribution and source f are given by equation(9). We apply $D_\parallel = 0$ on the half line of the domain for the VF scheme with $e = \Delta s$. For the time-integration we use the Crank-Nicolson scheme. The analytical solution (see Chacón et al. [4]) is given by

$$T(x, y, t) = \frac{1 - \exp\left(-2D_\perp \pi^2 t\right)}{D_\perp} \cos \pi x \cos \pi y. \tag{11}$$

In figure 21 we show the temporal value of the infinity error norm for an anisotropy level of $\varsigma = 10^6$. It is clear from the figure that setting $D_\parallel$ to zero on the half line greatly improves the accuracy, the accuracy for the 32×32 grid is comparable to the result by Chacón et al. [4].

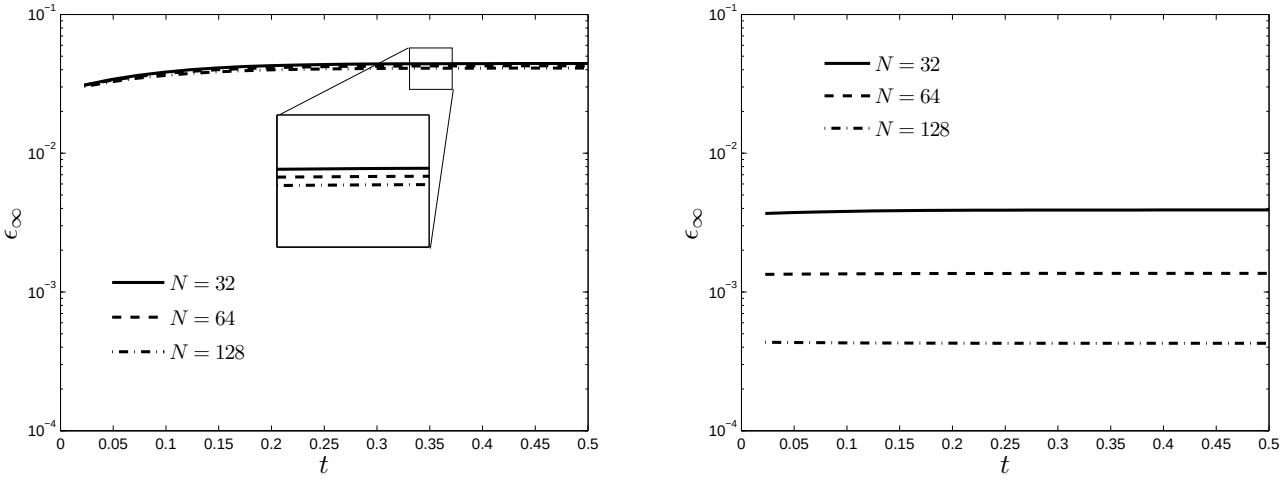

(a) (b)

Figure 21: Error ϵ_∞ for unsteady test case(11) using the VF scheme with Vandermonde coefficients, $e = \Delta s$, $\Delta t = 1/400$, $\varsigma = 10^6$, (a) without adaptation, (b) with $D_{\|} = 0$ on the half line $x = 0, y > 0$.

5 Conclusion

The motivation for this research was that $\mathcal{C}_1$ continuous connections of each volume with all of its nine neighbouring volumes would improve the accuracy for large values of the anisotropy. To have varying connectivity we introduced a parameter e. For $0 < e < \sqrt{2}h$ we have octogonal and quadrilateral volumes connected with each other. The results indicate that connectivity plays a role in the accuracy. For all test cases the optimal result in terms of convergence was obtained for either $e = 0$ or $e = \sqrt{2}h$, which is equivalent to the symmetric scheme. The connectivity as such is not of primary importance for maintaining the convergence and accuracy for the extreme anisotropy. Since a variation in e does not require any regridding, it may be beneficial for an unsteady problem to adapt the value of e based on previous timesteps. An extension to three dimensions is possible.

We further conclude that $D_{\|} = 0$ enforcement is a viable approach to improve numerical methods in case of extremely anisotropic problems with closed field lines and zero parallel diffusion. Inserting $D_{\|} = 0$ on a line connecting the O-point with the last closed field line recovers the formal accuracy in all the test problems described in this paper, including the Sovinec test case and the tilted elliptic test case. We also conclude that having a temperature unknown exactly in the O-point can improve the anisotropy independence significantly in case of closed field lines.

Acknowledgments

This work, supported by NWO and the European Communities under the contract of the Association EURATOM/FOM, was carried out within the framework of the European Fusion Program. The views and opinions expressed herein do not necessarily reflect those of the European Commission.

A Taylor expansions

For the **Asymmetric Scheme** described in section 2.1 the local truncation errors of the different terms are found by writing out the Taylor expansions

$$(D_{11}T_x)_x : T_x D_{11_x} + T_{xx} D_{11} + h^2 \left[\frac{1}{24} T_x D_{11_{xxx}} + \frac{1}{8} T_{xx} D_{11_{xx}} + \frac{1}{6} T_{xxx} D_{11_x} + \frac{1}{24} T_{xxxx} D_{11} \right] + \mathcal{O}(h^4),$$

$$(D_{21}T_y)_x : T_y D_{21_x} + T_{xy} D_{21} + h^2 \left[\frac{1}{24} T_y D_{21_{xxx}} + \frac{1}{144} T_{yyy} D_{21_x} + \frac{1}{8} T_{xy} D_{21_{xx}} + \frac{1}{6} T_{xyyy} D_{21} + \frac{1}{6} T_{xxxy} D_{21} + \frac{1}{4} T_{xxy} D_{21_x} \right] + \mathcal{O}(h^4),$$

and similarly for $(D_{22}T_y)_y$ and $(D_{21}T_x)_y$ respectively. Likewise for the **Symmetric Scheme** found in section 2.2 the approximations are given by

$$(D_{11}T_x)_x : T_x D_{11_x} + T_{xx} D_{11} + h^2 \left[T_x \left(\frac{1}{8} D_{11_{xyy}} + \frac{1}{24} D_{11_{xxx}} \right) + T_{xx} \left(\frac{1}{8} D_{11_{yy}} + \frac{1}{8} D_{11_{xx}} \right) + \frac{1}{4} T_{xy} D_{11_{xy}} + \frac{1}{4} T_{xyy} D_{11_x} + \frac{1}{4} T_{yyx} D_{11_y} + \frac{1}{6} T_{xxx} D_{11_x} + \frac{1}{4} T_{xxyy} D_{11} + \frac{1}{12} T_{xxxx} D_{11} \right] + \mathcal{O}(h^4),$$

$$(D_{21}T_y)_x : T_y D_{21_x} + T_{xy} D_{21} + h^2 \left[T_y \left(\frac{1}{8} D_{21_{xyy}} + \frac{1}{24} D_{21_{xxx}} \right) + T_{xy} \left(\frac{1}{8} D_{21_{yy}} + \frac{1}{8} D_{21_{xx}} \right) + \frac{1}{4} T_{yy} D_{21_{xy}} + \frac{1}{24} T_{yyy} D_{21_x} + \frac{1}{16} T_{xyy} D_{21_y} + \frac{1}{16} T_{yxx} D_{21_x} + \frac{1}{6} T_{xyyy} D_{21} + \frac{1}{6} T_{yxxx} D_{21} \right] + \mathcal{O}(h^4),$$

and similarly for $(D_{22}T_y)_y$ and $(D_{21}T_x)_y$ respectively.

B Interpolation Coefficients

Given an interpolation for T

$$T(x,y) = \sum_{i=0}^{2}\sum_{j=0}^{2}\gamma_{ij}x^i y^j, \tag{12}$$

the coefficients γ_{ij} follow from

$$\begin{pmatrix} \gamma_{22} \\ \gamma_{21} \\ \gamma_{12} \\ \gamma_{20} \\ \gamma_{02} \\ \gamma_{11} \\ \gamma_{10} \\ \gamma_{01} \\ \gamma_{00} \end{pmatrix} = \mathbf{V}^{-1}\mathbf{T}, \quad \mathbf{V} = \begin{pmatrix} h^4 & h^3 & -h^3 & h^2 & h^2 & -h^2 & -h & h & 1 \\ h^4 & h^3 & h^3 & h^2 & h^2 & h^2 & h & h & 1 \\ h^4 & -h^3 & -h^3 & h^2 & h^2 & h^2 & -h & -h & 1 \\ h^4 & -h^3 & h^3 & h^2 & h^2 & -h^2 & h & -h & 1 \\ 0 & 0 & 0 & h^2 & 0 & 0 & -h & 0 & 1 \\ 0 & 0 & 0 & h^2 & 0 & 0 & h & 0 & 1 \\ 0 & 0 & 0 & 0 & h^2 & 0 & 0 & h & 1 \\ 0 & 0 & 0 & 0 & h^2 & 0 & 0 & -h & 1 \\ 0 & 0 & 0 & 0 & 0 & 0 & 0 & 0 & 1 \end{pmatrix}, \quad \mathbf{T} = \begin{pmatrix} T_{i-1,j+1} \\ T_{i+1,j+1} \\ T_{i-1,j-1} \\ T_{i+1,j-1} \\ T_{i-1,j} \\ T_{i+1,j} \\ T_{i,j+1} \\ T_{i,j-1} \\ T_{i,j} \end{pmatrix},$$

and are given by

$$\begin{aligned}
\gamma_{22} &= \frac{1}{h^4}\left(T_{i,j} - \frac{T_{i,j-1}}{2} - \frac{T_{i-1,j}}{2} - \frac{T_{i+1,j}}{2} - \frac{T_{i,j+1}}{2} + \frac{T_{i-1,j-1}}{4} + \frac{T_{i+1,j-1}}{4} + \frac{T_{i+1,j+1}}{4} + \frac{T_{i-1,j+1}}{4}\right), \\
\gamma_{21} &= \frac{1}{4h^3}\left(2T_{i,j-1} - 2T_{i,j+1} + T_{i-1,j+1} + T_{i+1,j+1} - T_{i-1,j-1} - T_{i+1,j-1}\right), \\
\gamma_{12} &= \frac{1}{4h^3}\left(2T_{i-1,j} - 2T_{i+1,j} + T_{i+1,j-1} + T_{i+1,j+1} - T_{i-1,j-1} - T_{i-1,j+1}\right), \\
\gamma_{20} &= \frac{1}{2h^2}\left(T_{i-1,j} - 2T_{i,j} + T_{i+1,j}\right), \quad \gamma_{02} = \frac{1}{2h^2}\left(T_{i,j-1} - 2T_{i,j} + T_{i,j+1}\right), \\
\gamma_{11} &= \frac{1}{4h^2}\left(T_{i-1,j-1} + T_{i+1,j+1} - T_{i+1,j-1} - T_{i-1,j+1}\right), \\
\gamma_{10} &= \frac{T_{i+1,j} - T_{i-1,j}}{2h}, \quad \gamma_{01} = \frac{T_{i,j+1} - T_{i,j-1}}{2h}, \\
\gamma_{00} &= T_{i,j},
\end{aligned} \tag{13}$$

which we call the *Vandermonde* coefficients. Note that the coefficients $\gamma_1, \ldots \gamma_8$ are all approximations of differential terms in point i, j,

$$\gamma_{ij} = \frac{1}{i!j!}\left(\frac{\partial}{\partial x}\right)^i \left(\frac{\partial}{\partial y}\right)^j T(x,y). \tag{14}$$

C Linear operator

For the determination of the linear operator we write,

$$\begin{aligned}
T_x(x,y) &= \frac{\partial}{\partial x}\left[a_{0,0}T_{i,j} + a_{1,0}T_{i+1,j} + a_{-1,0}T_{i-1,j} + a_{0,1}T_{i,j+1} + a_{0,-1}T_{i,j-1}\right.\\
&\quad \left. + a_{1,1}T_{i+1,j+1} + a_{-1,1}T_{i-1,j+1} + a_{1,-1}T_{i+1,j-1} + a_{-1,-1}T_{i-1,j-1}\right],\\
T_y(x,y) &= \frac{\partial}{\partial y}\left[a_{0,0}T_{i,j} + a_{1,0}T_{i+1,j} + a_{-1,0}T_{i-1,j} + a_{0,1}T_{i,j+1} + a_{0,-1}T_{i,j-1}\right.\\
&\quad \left. + a_{1,1}T_{i+1,j+1} + a_{-1,1}T_{i-1,j+1} + a_{1,-1}T_{i+1,j-1} + a_{-1,-1}T_{i-1,j-1}\right],
\end{aligned}$$

where the operators $\frac{\partial}{\partial x}, \frac{\partial}{\partial y}$ only work on the coefficients $a_{k,l}$, $k,l = -1,0,1$, with x, y centered around i, j, where for the Vandermonde coefficients we have

$$\begin{aligned}
a_{0,0} &= \frac{x^2y^2}{h^4} - \frac{x^2}{h^2} - \frac{y^2}{h^2} + 1,\\
a_{\pm1,0} &= \frac{1}{2}\left(-\frac{x^2y^2}{h^4} \mp \frac{y^2x}{h^3} + \frac{x^2}{h^2} \pm \frac{x}{h}\right),\\
a_{0,\pm1} &= \frac{1}{2}\left(-\frac{x^2y^2}{h^4} \mp \frac{x^2y}{h^3} + \frac{y^2}{h^2} \pm \frac{y}{h}\right),\\
a_{\pm1,1} &= \frac{1}{4}\left(\frac{x^2y^2}{h^4} + \frac{x^2y}{h^3} \pm \frac{y^2x}{h^3} \pm \frac{xy}{h^2}\right),\\
a_{\pm1,-1} &= \frac{1}{4}\left(\frac{x^2y^2}{h^4} - \frac{x^2y}{h^3} \pm \frac{y^2x}{h^3} \mp \frac{xy}{h^2}\right).
\end{aligned} \tag{15}$$

Using the expressions for α given in equation(7) the contributions of the local symmetric coefficients to the linear operator are given by

$$\begin{aligned}
\frac{\partial}{\partial x}a_{0,0} &= \frac{1}{2h}\left(-\alpha_{ru} + \alpha_{lu} + \alpha_{ld} - \alpha_{rd}\right), & \frac{\partial}{\partial y}a_{0,0} &= \frac{1}{2h}\left(-\alpha_{ru} - \alpha_{lu} + \alpha_{ld} + \alpha_{rd}\right),\\
\frac{\partial}{\partial x}a_{1,0} &= \frac{1}{2h}\left(\alpha_{ru} + \alpha_{rd}\right), & \frac{\partial}{\partial y}a_{1,0} &= \frac{1}{2h}\left(-\alpha_{ru} + \alpha_{rd}\right),\\
\frac{\partial}{\partial x}a_{-1,0} &= \frac{1}{2h}\left(-\alpha_{lu} - \alpha_{ld}\right), & \frac{\partial}{\partial y}a_{-1,0} &= \frac{1}{2h}\left(-\alpha_{lu} + \alpha_{ld}\right),\\
\frac{\partial}{\partial x}a_{0,1} &= \frac{1}{2h}\left(-\alpha_{ru} + \alpha_{lu}\right), & \frac{\partial}{\partial y}a_{0,1} &= \frac{1}{2h}\left(\alpha_{ru} + \alpha_{lu}\right),\\
\frac{\partial}{\partial x}a_{0,-1} &= \frac{x}{2h}\left(\alpha_{ld} - \alpha_{rd}\right), & \frac{\partial}{\partial y}a_{0,-1} &= \frac{1}{2h}\left(-\alpha_{ld} - \alpha_{rd}\right),\\
\frac{\partial}{\partial x}a_{1,1} &= \frac{\alpha_{ru}}{2h}, & \frac{\partial}{\partial y}a_{1,1} &= \frac{\alpha_{ru}}{2h},\\
\frac{\partial}{\partial x}a_{-1,1} &= -\frac{\alpha_{lu}}{2h}, & \frac{\partial}{\partial y}a_{-1,1} &= \frac{\alpha_{lu}}{2h},\\
\frac{\partial}{\partial x}a_{1,-1} &= \frac{\alpha_{rd}}{2h}, & \frac{\partial}{\partial y}a_{1,-1} &= -\frac{\alpha_{rd}}{2h},\\
\frac{\partial}{\partial x}a_{-1,-1} &= -\frac{\alpha_{ld}}{2h}, & \frac{\partial}{\partial x}a_{-1,-1} &= -\frac{\alpha_{ld}}{2h}.
\end{aligned} \tag{16}$$

References

[1] I. Aavatsmark, T. Barkve, Ø. Bøe, and T. Mannseth. Discretization on non-orthogonal, quadrilateral grids for inhomogeneous, anisotropic media. *J. Comput. Phys.*, 127:2–14, 1996.

[2] I. Aavatsmark, T. Barkve, Ø. Bøe, and T. Mannseth. Discretization on unstructured grids for inhomogeneous, anisotropic media. part I: Derivation of the methods. *SIAM J. Sci. Comput.*, 19(5):1700–1716, 1998.

[3] J. Breil and P.-H. Maire. A cell-centered diffusion scheme on two-dimensional unstructured meshes. *J. Comput. Phys.*, 224:785–823, 2007.

[4] L. Chacón, D. del Castillo-Negrete, and C.D. Hauck. An asymptotic-preserving semi-Lagrangian algorithm for the time-dependent anisotropic heat transport equation. *J. Comput. Phys.*, 272:719–746, 2014.

[5] Y. Coudière, J.-P. Vila, and P. Villedieu. Convergence rate of a finite volume scheme for a two dimensional convection-diffusion problem. *ESAIM Math. Model. Numer. Anal.*, 33(3):493–516, 1999.

[6] J. Droniou. Finite volume schemes for diffusion equations: introduction to and review of modern methods. *HAL report hal-00813613*, 2013.

[7] M.G. Edwards and C.F. Rogers. Finite volume discretization with imposed flux continuity for the general tensor pressure equation. *Comput. Geosci.*, 2:259–290, 1998.

[8] J.H. Ferziger and M. Perić. *Computational Methods for Fluid Dynamics*. Springer, 2002.

[9] S. Günter, Q. Yu, J. Krüger, and K. Lackner. Modelling of heat transport in magnetised plasmas using non-aligned coordinates. *J. Comput. Phys.*, 209:354–370, 2005.

[10] F. Hermeline. A finite volume method for the approximation of diffusion operators on distorted meshes. *J. Comput. Phys.*, (160):481–499, 2000.

[11] J. Hyman, M. Shashkov, and S. Steinberg. The numerical solution of diffusion problems in strongly heterogeneous non-isotropic materials. *J. Comput. Phys.*, 132:130–148, 1997.

[12] P. Jacq, P.H. Maire, and R. Abgrall. A high-order cell-centered finite volume scheme for simulating three dimensional anisotropic diffusion equations on unstructured grids. *HAL report hal-00835537*, 2013.

[13] C. Le Potier. Schéma volumes finis monotone pour des opérateurs de diffusion fortement anisotropes sur des maillages de triangles nonstructurés. *C.R. Math.*, 341(12):787–792, 2005.

[14] C. Le Potier and T.H. Ong. A cell-centered scheme for heterogeneous anisotropic diffusion problems on general meshes. *Int. J. Finite Vol.*, 8:1–40, 2012.

[15] K. Lipnikov, M. Shashkov, D. Svyatskiy, and Y. Vassilevski. Monotone finite volume schemes for diffusion equations on unstructured triangular and shape-regular polygonal meshes. *J. Comput. Phys.*, 227:492–512, 2007.

[16] P.-H. Maire and J. Breil. A high-order finite volume cell-centered scheme for anisotropic diffusion on two-dimensional unstructured grids. *J. Comput. Phys.*, 224(2):785–823, 2011.

[17] J.E. Morel, R.M. Roberts, and M. Shashkov. A local support-operators diffusion discretization scheme for quadrilateral $r - z$ meshes. *J. Comput. Phys.*, 144:17–51, 1998.

[18] P. Sharma and G.W. Hammett. Preserving monotonicity in anisotropic diffusion. *J. Comput. Phys.*, 227:123–142, 2007.

[19] M. Shashkov and S. Steinberg. Support-operator finite-difference algorithms for general elliptic problems. *J. Comput. Phys.*, 118:131–151, 1995.

[20] C.R. Sovinec, A.H. Glasser, T.A. Gianakon, D.C. Barnes, R.A. Nebel, S.E. Kruger, D.D. Schnack, S.J. Plimpton, A. Tarditi, and M.S. Chu. Nonlinear magnetohydrodynamics simulation using high-order finite elements. *J. Comput. Phys.*, 195:355–386, 2004.

[21] M.V. Umansky, M.S. Day, and T.D. Rognlien. On numerical solution of strongly anisotropic diffusion equation on misaligned grids. *Numer. Heat Transf., Part B.*, 47:533–554, 2005.

[22] B. van Es, B. Koren, and H.J. de Blank. Finite-difference schemes for anisotropic diffusion. *J. Comput. Phys.*, 272:1–24, 2014.